

# Structural window frame for in-plane seismic strengthening of masonry wall buildings

Jorge Miguel Proença, António S. Gago & André Vilas Boas

To cite this article: Jorge Miguel Proença, António S. Gago & André Vilas Boas (2019) Structural window frame for in-plane seismic strengthening of masonry wall buildings, International Journal of Architectural Heritage, 13:1, 98-113, DOI: [10.1080/15583058.2018.1497234](https://doi.org/10.1080/15583058.2018.1497234)

To link to this article: <https://doi.org/10.1080/15583058.2018.1497234>



Published online: 07 Aug 2018.



Submit your article to this journal [↗](#)





Article views: 28



View Crossmark data [↗](#)



## Structural window frame for in-plane seismic strengthening of masonry wall buildings

Jorge Miguel Proença , António S. Gago , and André Vilas Boas

IST – U Lisboa, CERIS, Lisbon, Portugal

### ABSTRACT

This article describes the initial development stages of a structural window frame system for the in-plane seismic strengthening of load-bearing masonry wall buildings. The solution implemented ultimately aims to stiffen (and strengthen) the opening such that the wall would behave as if there were no opening. This is achieved by installing a structural steel window frame composed of a profile forming a closed ring inside the opening, properly tied to the surrounding masonry wall. The strengthening concept was validated by means of a series of tests in which two approximately 1:2 geometric scale physical specimens with a similar central opening were cyclically tested to failure. One of these specimens (UMW) was unreinforced whereas the other (RMW) had a UPN profile internal ring tied at the corners and at mid-length and mid-height of the opening by means of threaded rods with chemical anchors. The material of these walls was common rubble masonry with lime-based mortar and render. The experimental results show that the strengthening technique leads to a significant increase in strength and in-plane deformation capacity, as well as in terms of cumulative dissipated energy at collapse. Nonlinear numerical specimens of the tested walls were also developed and calibrated.

### ARTICLE HISTORY

Received 12 March 2018  
Accepted 24 May 2018

### KEYWORDS

Earthquakes; experimental tests; masonry wall buildings; nonlinear analyses; seismic window frame; strengthening

### Introduction

In most southern European earthquake-prone cities, such as those in Portugal, especially Lisbon (Simões et al. 2017), the building stock comprises a large number of old unreinforced masonry buildings, built before the enforcement of structural codes to ensure earthquake-resistance. The main structural elements that withstand earthquakes in buildings of this type are the unreinforced masonry walls that make up the vertical loadbearing structure, tied at storey level by the generally wooden floor structures. These buildings were empirically designed only to withstand gravity loads and were therefore seismically vulnerable in view of our current knowledge. The major flaws of that structural system have been consistently highlighted in previous earthquake occurrences, in particular in terms of the weaknesses associated with the out-of-plane and in-plane behavior of the masonry walls, lack of in-plane stiffness of the floor structures and insufficient connection between walls and floors. Assuming that the out-of-plane behavior of the load-bearing masonry walls is not critical (e.g., because they are properly tied to not excessively spaced perpendicular walls, either by means of block imbrication or by the installation of special

connecting devices), the focus on of the earthquake resistance of the building lies in the in-plane behavior of the load-bearing masonry walls. In this case, the existence of openings tends to concentrate damage in the piers and therefore may precipitate the collapse of the building.

The seismic strengthening of a load-bearing masonry wall building may involve deploying different available or innovative strengthening techniques, of which the one presented here is an example. Each such technique is designed to tackle one or more of the sources of fragility identified. The choice of technique may ultimately be governed by cost-benefit considerations (Marques et al. 2017).

Whereas significant research has been conducted and reported for strengthening solid masonry walls (typically through the addition of reinforced render layers on both faces), much less work has looked at retrofitting perforated masonry walls, that is, walls with openings such as windows or doors. One study was carried out by Kalali and Kabir (2012) who evaluated the cyclic behavior of perforated brick masonry walls strengthened with glass fiber reinforced polymers. They studied the effect of different quantities, types, and

**CONTACT** Jorge Miguel Proença  [jorge.m.proenca@tecnico.ulisboa.pt](mailto:jorge.m.proenca@tecnico.ulisboa.pt)  Universidade de Lisboa Instituto Superior Tecnico, DECivil Av. Rovisco Pais nº 1, Lisboa, 1049-001, Portugal.

Color versions of one or more of the figures in the article can be found online at [www.tandfonline.com/uarc](http://www.tandfonline.com/uarc).

© 2018 Taylor & Francis

layouts of the FRP used. Work by Vanin and Foraboschi (2012) has shown that the arrangement of bricks in the spandrels and piers strongly influences the failure modes for in-plane shear forces.

The objective of this study is to evaluate the feasibility of in-plane strengthening of load-bearing masonry walls with windows and doors by installing a structural steel window frame inside the openings in question. The strengthening concept is based on the observation that the existence of openings in exterior load-bearing masonry walls often favors the formation of in-plane collapse mechanisms, leading to the collapse of the whole building. The main assumption of this research is that the insertion of stiffening steel rings inside the openings might modify and delay the collapse mechanisms to such an extent that they are no longer critical. To confirm the main assumption, experiments were carried out in which two rubble stone masonry walls, one unreinforced and the other reinforced, with identical openings, were cyclically tested to failure. The strengthening concept was tested (and validated) for single-leaf rubble masonry walls but the authors believe that this concept could be extended to other types of single-leaf masonry walls (e.g., clay brick masonry walls). Nonlinear finite element specimens of both walls were also developed and calibrated using DIANA 9.2 software (De Witte and Kikstra 2007) with a view to enabling parametric studies to be carried out in the future. This research was the subject of an M. Sc. dissertation (Vilas Boas 2017).

### In-plane collapse mechanisms of masonry walls

When a load-bearing masonry wall is subjected to in-plane forces, the existence of openings allows the entire wall to be divided into pier and spandrel elements. In-plane stiffness and the type of connection of the floor structures to the wall further divides the piers into panels that consist of the parts of the piers laterally bounded by the openings. The prevailing collapse mechanism can be one of many and largely depends

on the geometry of the openings, which influences the geometry of the panel and spandrel elements, and the vertical loading on the subdivided elements. Nevertheless, three major structural specimens associated with collapse mechanisms can be identified for the wall as a whole (Mendes and Lourenço 2015, 139–164): (i) cantilever walls connected by flexible floors; (ii) coupled walls with pier hinging; and (iii) coupled walls with spandrel hinging. The prevailing structural model/collapse mechanism is ultimately determined by the strength of the panel and spandrel elements.

Load-bearing masonry wall panels subjected to in-plane lateral and vertical loading may typically show two types of behavior, flexural and/or shear behavior, each with its own associated failure modes. The behavior induced by the out-of-plane loading, not covered in this study, has some similarities with the flexural behavior, in this case greatly worsened in view of the residual tensile strength of the masonry material.

In flexural behavior, the mode of failure depends on the level of vertical load applied. If it is low compared to the compressive strength, the horizontal load produces tensile flexural cracking at the corners and the wall begins to behave like a nearly rigid body rotating around the compressed corner—rocking. On the other hand, if the applied vertical load is sufficiently high, the masonry located at the compressed corner may be crushed—*toe crushing*.

In shear behavior, the horizontal load may produce two different modes of failure: sliding shear failure, in which the development of flexural cracking at the corners under tension reduces the resisting section and failure occurs with sliding on a horizontal bed joint plane; and diagonal cracking, when failure is caused by the formation of a diagonal crack. This typically develops at the centre of the wall and then propagates towards the corners, as concluded in NIKER (POLIMI 2010). Three failure modes are depicted in Figure 1.

The above interpretation of the types of behavior of load-bearing masonry wall panels can be extended to

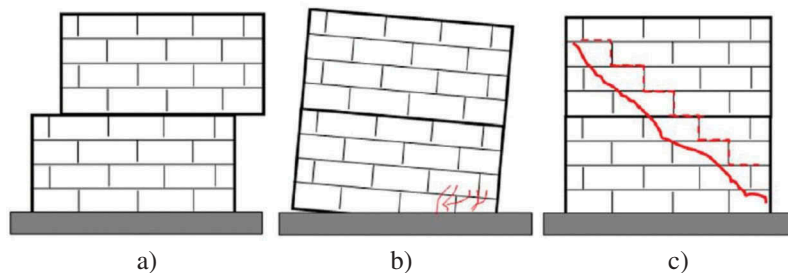


**Figure 1.** Typical in-plane failure modes of masonry walls: (a) sliding shear failure; (b) rocking; and (c) diagonal cracking (Cakir et al. 2015).

the behavior of the spandrel elements, noting that these are rotated 90°, such that their axis is horizontal instead of vertical, and subjected to reduced normal stresses.

It is believed that the existence of a stiffening element within the opening could lead to increased interaction between the behavior of the different wall panels (pier and spandrel) into which the wall is divided, possibly changing the prevailing failure mode and increasing the associated lateral strength.

### In-plane behavior of the structural window frame

Openings in load-bearing masonry wall buildings can be regarded as sources of fragility because of their in-plane behavior. Therefore, the strengthening solution under development ultimately aims to stiffen and strengthen the opening so that the wall should behave as if there were no opening. In other words, the internal stiffness of the steel ring, computed according to the tying system between the ring and surrounding masonry, should ultimately provide an additional stiffness ( $K^*$ ) comparable to that of the removed part of the wall (here considered equivalent to the stiffness of the diagonal masonry strut of a wall with the same dimensions as the opening,  $K$ ).

To simulate the effects of different connection systems between the steel ring and the surrounding masonry, three different rectangular frame linearly elastic models were studied: Model A in which the rotation is released in every node, Model B in which the rotation is restrained in every node, and Model C in which the rotation is released in every node but restrained at mid-height of the vertical steel profiles. These three models correspond to possible connection details between the steel ring and the surrounding masonry, e.g., in terms of the location and number of the post-installed anchor bolt or rod devices that could be used for the connection.

The masonry strut model adopted and the different steel ring models analysed are presented in [Figure 2](#), where  $b$  and  $h$  correspond to the width and height, respectively of the opening,  $q_i$  corresponds to the structure's degrees of

freedom,  $F$  is the in-plane horizontal force applied to the structure,  $L$  is the length of the diagonal masonry strut, and  $\alpha$  is the angle between the strut and the horizontal. Note that the cross-sectional area of the masonry strut was assumed to be equal to the product of the wall thickness ( $t$ ) and the width of the strut, here taken as 15% of the strut length as suggested in the background document of Eurocode 8, Part 1 (Fardis et al., 2005).

The horizontal stiffness of the masonry strut model is given by Eq. (1) and the horizontal stiffness of the different steel ring connection models analysed is given by Eqs. (2), (4) and (6), where  $E_{masonry}$  represents the Young's modulus of the masonry and  $E_{steel}$  represents the Young's modulus of the steel profile. The derivation of Eqs. (2), (4), and (6) was based on the static condensation, or Guyan reduction, of the stiffness matrices, taking the top horizontal displacement ( $q_1$ ) as the independent (master) degree of freedom. Once those expressions have been derived it is possible to evaluate the minimum required flexural inertia  $I$  of the steel profiles so that the reinforced perforated wall behaved as if there were no opening. The simplified expressions are presented in Eqs. (3), (5), and (7):

$$K = E_{masonry} 0.15t \frac{b^2}{b^2 + h^2} \quad (1)$$

Model A:

$$K_A^* = E_{steel} I \frac{24}{h^2(b+h)} \quad (2)$$

$$I = \frac{E_{masonry}}{E_{steel}} 0.15t \frac{b^2 h^2 (b+h)}{24(b^2 + h^2)} \quad (3)$$

Model B:

$$K_B^* = E_{steel} I \frac{24}{h^3} \quad (4)$$

$$I = \frac{E_{masonry}}{E_{steel}} 0.15t \frac{b^2 h^3}{24(b^2 + h^2)} \quad (5)$$

Model C:

$$K_C^* = E_{steel} I \frac{192(b+3h)}{h^3(4b+3h)} \quad (6)$$

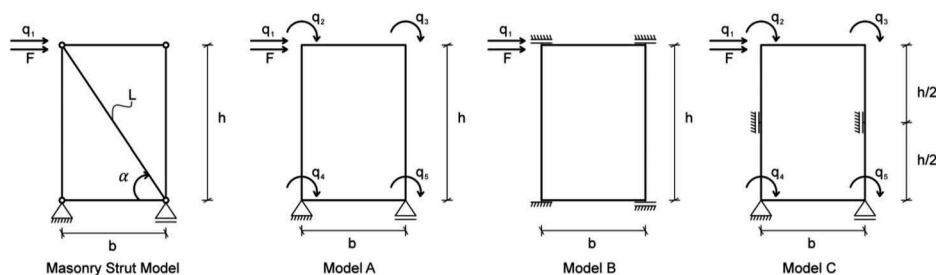


**Figure 2.** Masonry strut model and the different steel ring models analyzed.

$$I = \frac{E_{masonry}}{E_{steel}} 0.15t \frac{b^2 h^3 (4b + 3h)}{192(b + 3h)(b^2 + h^2)} \quad (7)$$

As expected, the minimum required flexural inertia of the steel profile greatly decreases when the constraints are increased, in terms of both their number (number of anchor bolts/rods) and their restraining detail (i.e., the possibility of also considering a rotation restriction at the connections).

### Characterization of the tested specimens

Two identical perforated rubble stone masonry walls were built to assess their behavior under static cyclic shear tests (Figure 3). Both walls were constructed over a 2.3 x 1.0 x 0.3 m reinforced concrete (RC) footing; their outside dimensions were 2.1 x 0.3 x 1.5 m and the dimensions of the openings, centred in the wall, were 0.5 x 0.3 x 0.75 m.

A 1.0 x 0.25 x 0.075 m concrete lintel was placed over the opening during construction to simulate the stone lintels typically used in these cases. An RC beam

(stiff beam) was cast over the top of the masonry wall to allow a more even distribution of the vertical load during tests. Figure 4a–c show the different construction stages of the walls.

The geometric physical scale specimens were made with Lioz stone, a type of limestone widely used in the past in Lisbon as an ornamental rock or as a structural material, for lintels and sills of window frames, or as capping, or even as stone units for rubble masonry. The mortar chosen was REABILITA CAL Reboco, which is a pre-mixed natural hydraulic lime mortar produced by Secil Argamassas. This product belongs to the class CSII according to the European standard EN 998–1 (IPQ 2010) and has a compressive strength of between 1.5 and 5.0 MPa (MIA 2015). As a reference, Cunha (Cunha 2013) determined that the compressive strength and flexural strength of REABILITA CAL Reboco were 1.70 MPa and 1.00 MPa, respectively. To meet the requirement of the mortar being as consistent as possible with that used in historical buildings, this strength was reduced by adding 5 kg of river sand for every 25 kg of mortar.

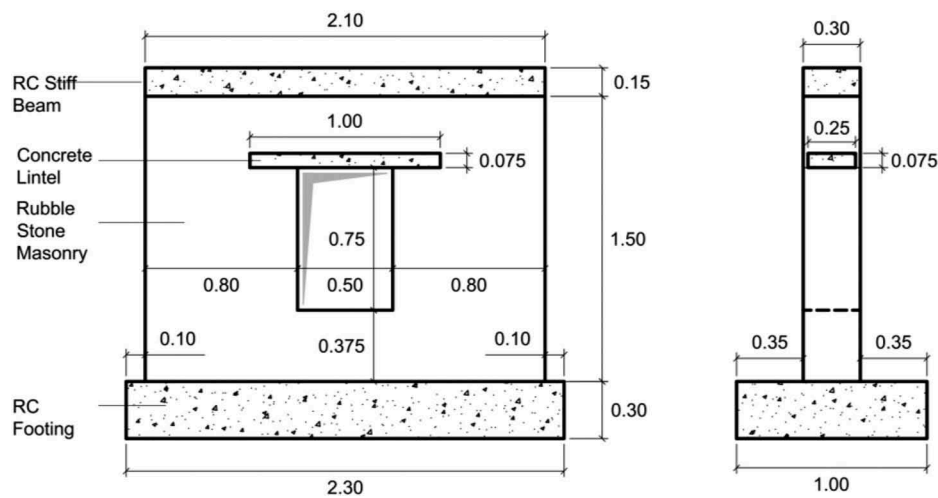


Figure 3. Geometry of the masonry walls specimens (dimensions in m).

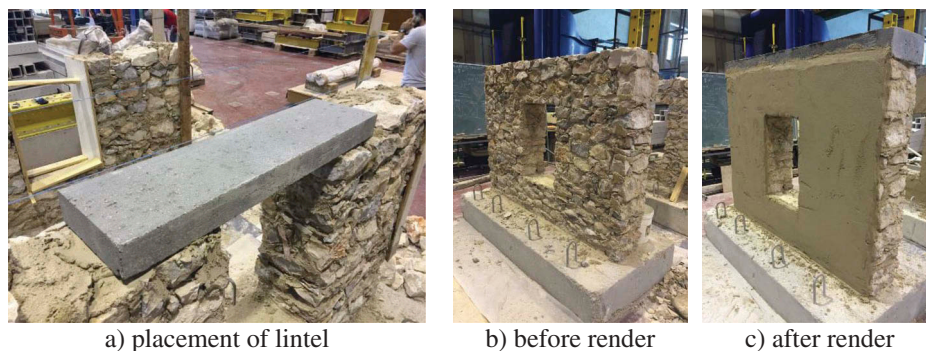


Figure 4. Construction stages of the specimen walls.



According to EN 1015–11:2007 (CEN 2007), six prismatic specimens of the weakened hydraulic mortar measuring  $160 \times 40 \times 40$  mm were tested. The average value of the flexural strength (mortar tensile strength obtained by bending tests) was 0.24 MPa and the average value of the compressive strength, determined by compression tests performed on the half-prisms yielded by the bending tests, was 0.50 MPa. Although somewhat lower, these results are comparable to those of natural hydraulic lime mortars used to obtain a realistic representation of a historical masonry with low-strength properties (Pelà, Roca, and Aprile 2017).

### Characterization of the strengthening solution

Referring to section 3, models A, B, and C for the same profile show an increasing restraining effect for the movements of the steel ring relative to the surrounding masonry. Assuming that the Young's modulus of common rubble masonry and steel is 1.64 GPa (Milosevic et al. 2013) and 210 GPa, respectively, the minimum required flexural inertia for the steel profile to achieve a stiffening effect similar to there being no opening would be  $316.8 \text{ cm}^4$  (model A),  $190.1 \text{ cm}^4$  (model B) and  $36.7 \text{ cm}^4$  (model C).

Since the wall specimens were built in a controlled environment (in the laboratory, with unimpeded access to all faces of the walls during the construction) it was possible to ensure that there were no significant voids inside the masonry, and thus the use of sleeves for the threaded rods was not necessary. The absence of sleeves meant a higher effective embedment depth, of around 200 mm was needed for the threaded rods in the injectable adhesive. The adopted injection system was HIT-HY 270, a high performance chemical anchor suitable for most common types of masonry materials and produced by HILTI.

### Cyclic shear-compression tests

The unreinforced masonry wall (UMW) and the reinforced masonry wall (RMW) underwent cyclic displacement-controlled testing to failure. The tests were carried out with a vertical stress of 0.2 MPa (126 kN), representing an average vertical stress due to dead loads at mid-height of an old masonry building. Thus, both walls were initially subjected to a vertical compression load which was kept constant for the remainder of the test. A stiff beam on the top of the walls was used to ensure a uniform distribution of the vertical load and a set of steel rollers were placed on the top of the walls to allow its horizontal displacement (Figure 6, the load being applied by the vertical jack). The horizontal

load was transmitted to the top of the wall by means of a system of steel plates that was firmly connected with high strength steel (HSS) threadbars. In order to prevent the wall footing from sliding, the reinforced concrete footing was fixed to the strong floor and reaction wall by a system of steel beams and horizontal pre-stressed HSS threadbars. The vertical load application system and a lateral frictionless guiding system were attached to a transverse steel frame (not shown in Figure 6).

The rotation of the footing was further restrained by clamping it with a set of perpendicular steel beams, which were vertically and manually pre-stressed (Figure 7).

The test instrumentation consisted in a set of 12 LVDT displacement transducers, a load cell for measuring the horizontal load applied by the actuator, and a set of 6 strain gauges installed on the steel profile forming the steel ring (in the RMW specimen).

Figure 8 illustrates the identification of the LVDT, of which d1, d10, and d11 were used to confirm that the RC footing clamping system was effective, d2, d3, and d12 measured the lateral displacement at different heights, d6–d9 measured the diagonal displacement in both piers and, finally, d4 and d5 measured the top rotation of the walls.

The 6 strain gauges were installed in groups of 3 in 2 cross sections of the steel ring, namely cross-section A, at  $\frac{3}{4}$  height in one of the vertical elements, and cross section B, at the quarter span point of the top horizontal element (these cross sections are identified in Figure 5). These strain gauges should allow the computation of the internal forces at the instrumented cross sections of the steel ring.

The top lateral displacement history measured by the controlling LVDT d12 roughly followed ASTM E2126-02a (ASTM 2002) Method B testing specifications. This method proposes a displacement history as a function of the ultimate displacement ( $\Delta_u$ ), consisting of two patterns of gradually increasing displacement amplitudes. In the first pattern, the amplitude is increased with each cycle until  $0.2\Delta_u$  is reached. In the second pattern, three cycles are applied at each amplitude until failure. The ultimate displacement was assumed to be 30 mm, corresponding to a 2% drift at the top of the wall. The horizontal displacement history and the numbering of the respective semi-cycles are presented in Figure 9.

The experimental tests were stopped when the measured horizontal load became less than 80% of the maximum registered horizontal load (post-peak behavior). Some of the test specifications described in this section are similar to those in the tests performed by Milosevic et al. (2015).

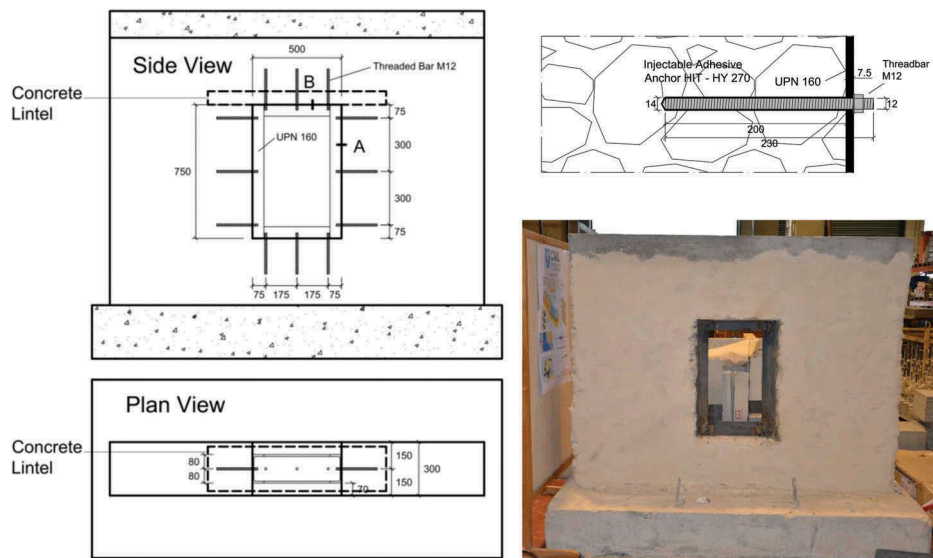


Figure 5. Characterization of the strengthening solution (dimensions in mm).

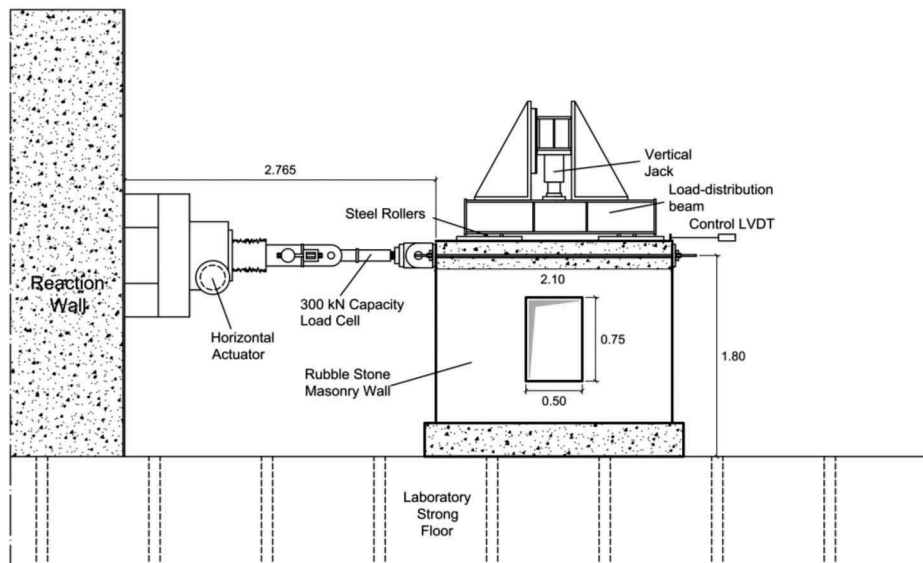


Figure 6. Vertical and horizontal load transmission systems (m).

## Experimental results

### Typical behavior and failure modes

#### Unreinforced masonry wall (UMW)

At displacements of around 6 mm, the first diagonal crack due to the shear mechanism appeared at the centre of both masonry piers. As the lateral force increased, the opening of these cracks progressed and the cracks propagated towards the top and bottom corners of the wall and towards the top and bottom corners of the opening.

The cyclic test of the unreinforced masonry wall ended when a + 24 mm horizontal displacement on the top of the wall (semi-cycle 29) was reached, for the

first time. The failure of the UMW was attributed to diagonal cracking in both masonry piers, which occurred along the stone-mortar interface. The crack pattern and the damage state of the UMW for a lateral displacement of -18 mm can be seen in Figure 10.

#### Reinforced masonry wall (RMW)

As with the UMW, the first diagonal crack appeared at the centre of both masonry piers at displacements of around 6 mm. With increasing imposed displacements, the formation of new cracks and extension of the existing ones continued.

The cyclic test of the reinforced masonry wall ended when a -30 mm horizontal displacement on the top of

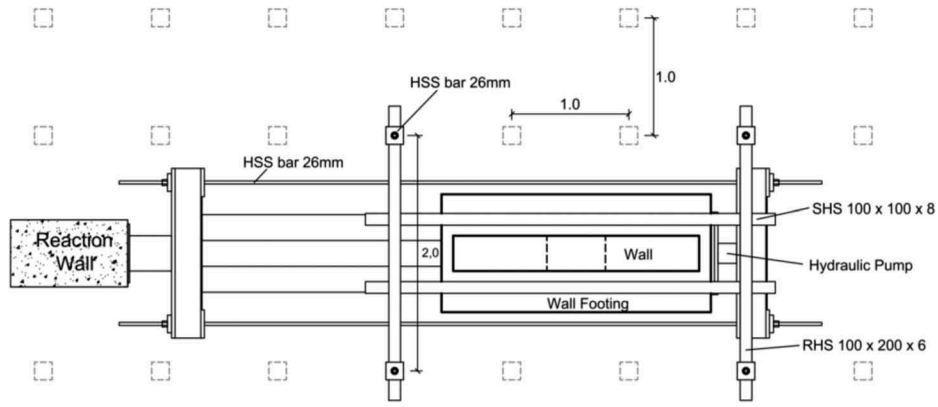


Figure 7. Wall footing clamping system (m).

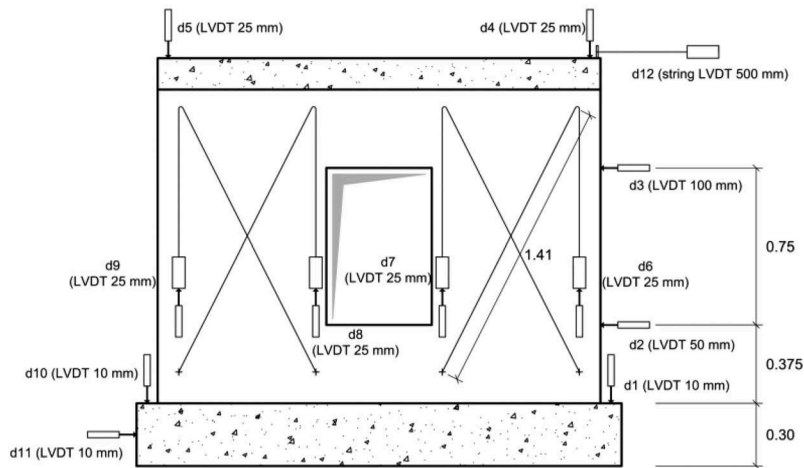


Figure 8. Identification, location and range of the LVDT (mm, m).

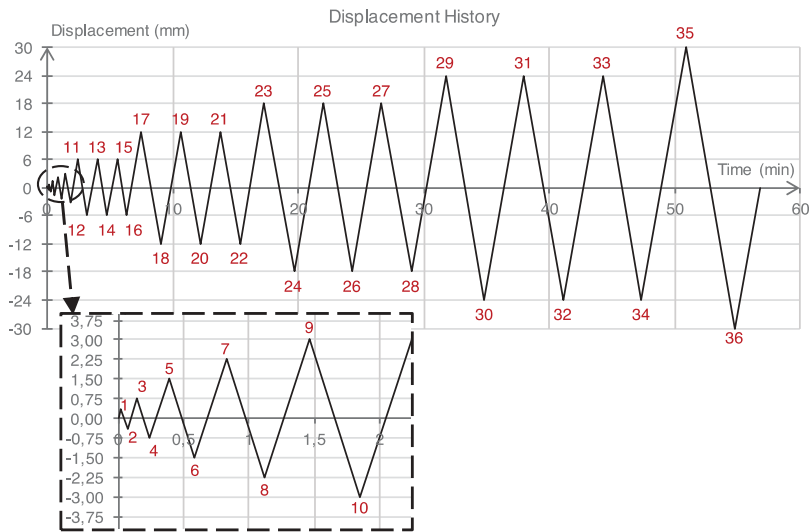


Figure 9. Displacement history (semi-cycles number and amplitude).

the wall (semi-cycle 36) was reached for the first time. The failure of the UMW was predominantly influenced by diagonal cracking in both masonry piers, although some rotation on the top of the wall and significant

horizontal cracks were noticed, two features usually attributed to rocking failure.

The installation of the UPN160 steel ring inside the opening and the way it was tied to the surrounding



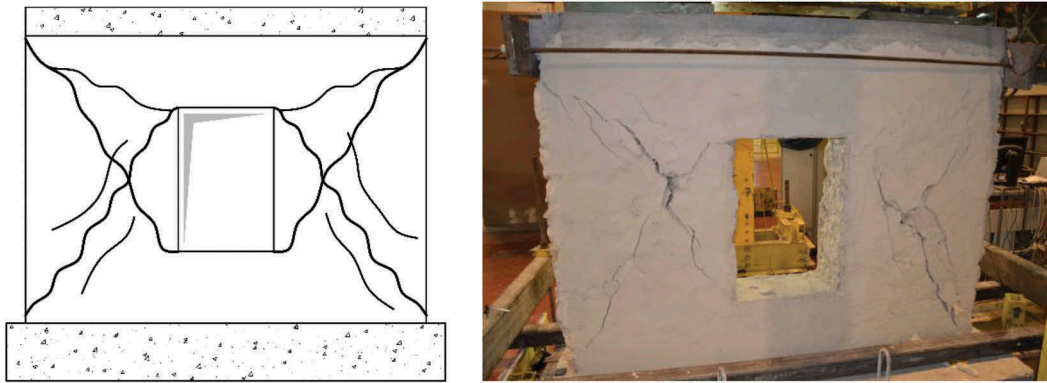


**Figure 10.** Crack pattern and the damage state of the UMW for a lateral displacement of  $-18$  mm.

masonry clearly influenced the crack pattern and the collapse mechanism. It is worth mentioning that the screws in the lower horizontal steel profile were loose at the end of the test (evidence of strong tensile forces in that region), and horizontal sliding of this steel profile was noticed (evidence of important shear forces at the steel-masonry interface). The crack pattern of the RMW and deformation of the strengthening solution for a lateral displacement of  $+18$  mm can be seen in Figure 11.

After the tests, some stone blocks which still seemed to be part of the walls were in fact detached from it and could be removed by hand. Also, a significant part of the render layer had come away from the masonry during the tests.

### **Hysteretic force-displacement diagrams**

In addition to the crack patterns and failure modes, the horizontal force–horizontal displacement diagrams provide valuable insight into the lateral in-plane behavior.

For the UMW, the maximum positive applied load was  $+70.41$  kN (horizontal displacement of  $+12$  mm). The maximum negative load was  $-71.59$  kN, at a horizontal displacement of  $-6$  mm. The cyclic response of

this wall showed some asymmetry, in particular at the level of the maximum lateral strength observed.

In the case of the RMW, the maximum positive applied load was  $+104.46$  kN, at a horizontal displacement of  $+12$  mm. The maximum negative applied load was  $-94.14$  kN, at a horizontal displacement of  $-12$  mm.

The UMW and RMW horizontal force vs. displacement hysteresis diagrams are presented in Figures 12 and 13. Comparing the hysteresis diagrams of the two walls, RMW clearly showed increased deformation capacity and horizontal in-plane strength relative to UMW. The improvements of the RMW in terms of peak strength were around 48% and 32%, respectively, for the positive and negative displacement directions, whereas the increase in the deformation capacity was 25%, from 24 to 30 mm.

### **Energy dissipation**

The integrity of a structure when subjected to an earthquake depends on its ability to dissipate the energy input from the ground motion. The estimation of the energy input is not straightforward but the increase in the capability of dissipating energy through stable

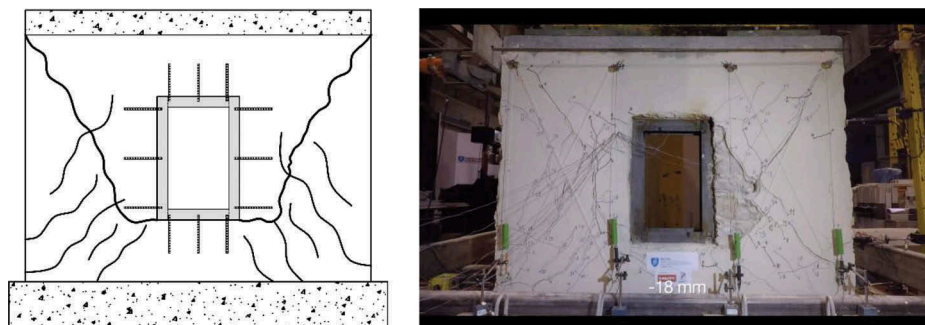


**Figure 11.** Crack pattern of the RMW and deformation of the strengthening solution for a lateral displacement of  $-18$  mm.

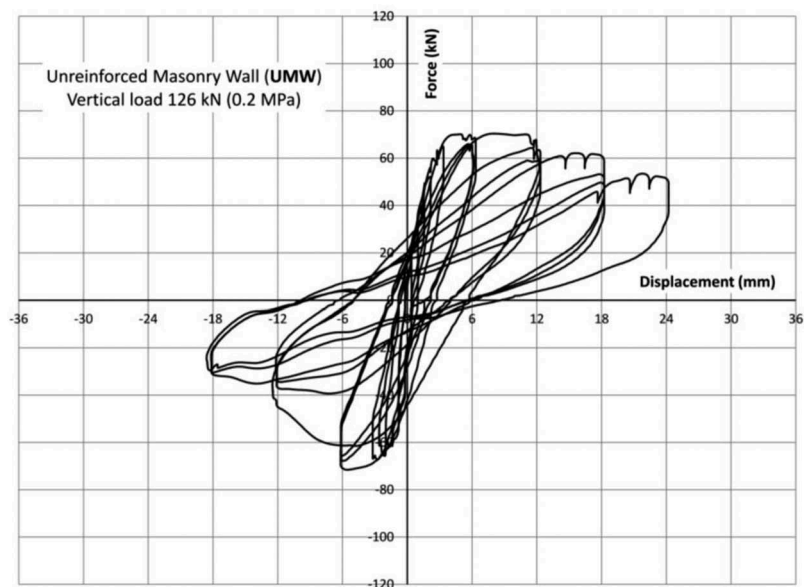


**Figure 12.** Horizontal force vs. control displacement hysteresis diagram for UMW specimen.

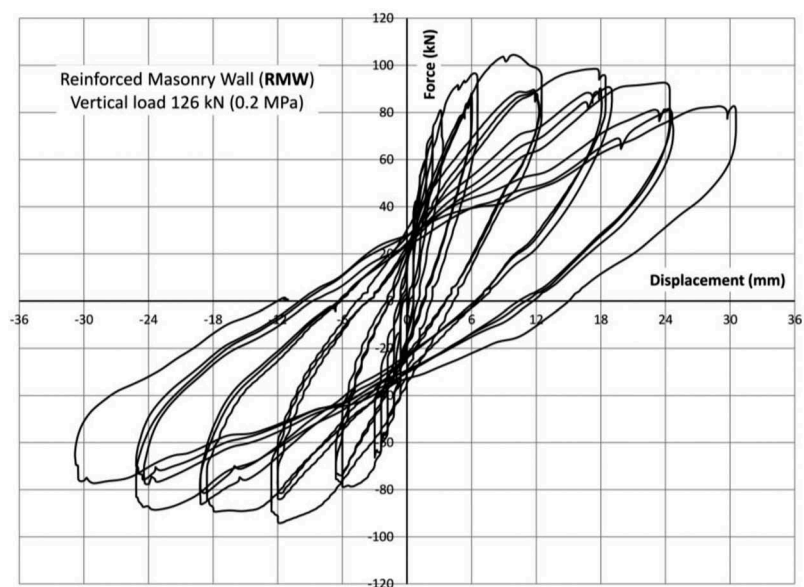


**Figure 13.** Horizontal force vs. control displacement hysteresis diagram for RMW specimen.

nonlinear behavior unquestionably reduces the seismic risk and vulnerability of a given structure.

The experimental tests can serve to assess the energy dissipation capabilities for different structural details. The energy dissipated in a cycle can be calculated as the area that the hysteretic loop encloses in the corresponding masonry wall top load-displacement plot. The cumulative energy dissipated by each specimen during the reversed cyclic load test was calculated by summing the energy dissipated in consecutive load-displacement loops throughout the tests. **Figure 14** depicts the evolution of the

cumulative dissipated energy over the cycles for both specimens.

The values of the total dissipated energy for specimens UMW and RMW were 8.55 kJ and 21.16 kJ, respectively, showing a 147% increase in the capacity of the wall to dissipate energy when strengthened.

Until semi-cycle 16, both walls dissipated roughly the same amount of energy, showing that the strengthening technique has no significant effect for reduced displacements (6 mm, drift of 0.4%). In reality, until that semi-cycle the increase in the strength exhibited by the RMW is compensated by the more significant nonlinear behavior

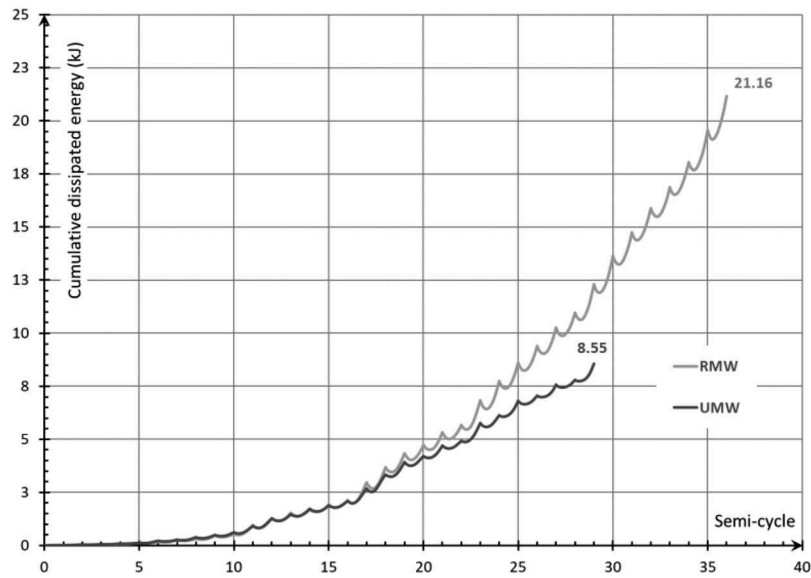


Figure 14. Cumulative dissipated energy for both specimens.

of the UMW, such as increased residual displacement, in such a way that the accumulated dissipated energy values are comparable. After that semi-cycle, the RMW managed to dissipate more energy and the difference between the UMW and RMW in terms of dissipated energy consistently increased until failure, which occurred later for the reinforced wall specimen.

#### Lateral deformation profile along height

The existence of the opening should influence the lateral deformation profiles along the height of the tested walls, possibly leading to a concentration of deformation along the height of the opening. To confirm this assumption, Figure 15 summarizes the lateral deformation profiles along the height at the end of semi-cycles 9, 11, and 17

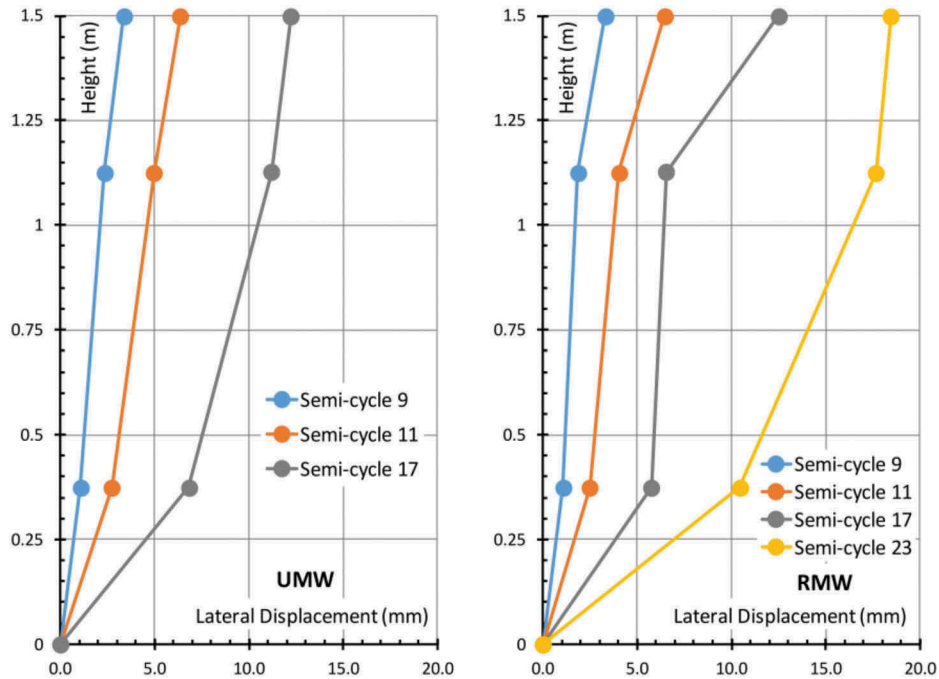
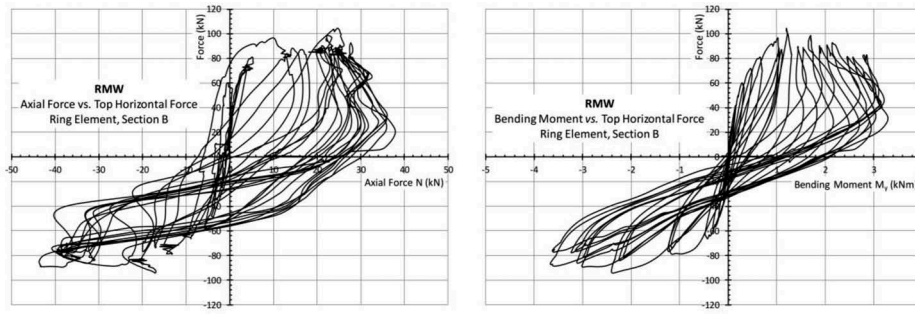


Figure 15. Lateral deformation profile: left (UMW) and right (RMW).



**Figure 16.** Internal forces in the steel ring profile (section B).

for both specimens, and 23 only for the RMW specimen. These lateral deformation profiles correspond to the measurements by LVDT 2, 3, and 12, installed at 0.375 m, 1.125 m, and 1.5 m above the RC footing.

Regardless of the semi-cycle considered, the lateral deformation profile of the UMW specimen shows a quasi-linear pattern along the height, with some concentration below the opening. For the same semi-cycles (9, 11, and 17) the lateral deformation increment of the RMW specimen along the height of the opening is quite small, demonstrating the effectiveness of the internal steel ring in stiffening the opening. Finally, at semi-cycle 23, the lateral deformation profile pattern of the RMW specimen resembles that of the UMW specimen in the previous semi-cycles, indicating that the stiffening effect has lost part of its effectiveness.

### Steel ring behavior

The steel ring was instrumented at two cross-sections, A and B, by means of groups of 3 strain gauges installed at known positions along the cross sections. The strain at the centroid ( $\varepsilon_G$ ) as well as of both curvatures ( $\chi_y$  and  $\chi_z$ , respectively, for bending along the weak and strong axes) for one of these cross sections can be computed according to Equation (8):

$$\begin{Bmatrix} \varepsilon_G \\ \chi_y \\ \chi_z \end{Bmatrix} = \begin{bmatrix} 1 & z_a & -y_a \\ 1 & z_b & -y_b \\ 1 & z_c & -y_c \end{bmatrix}^{-1} \begin{Bmatrix} \varepsilon_a \\ \varepsilon_b \\ \varepsilon_c \end{Bmatrix} \quad (8)$$

In which  $\varepsilon_a$ ,  $\varepsilon_b$ , and  $\varepsilon_c$  are the strains measured at the three positions, a–c, whose cross-sectional coordinates are  $(y_a, z_a)$ ,  $(y_b, z_b)$ , and  $(y_c, z_c)$ .

Assuming Euler-Bernoulli hypotheses and considering linear elastic behavior, the axial force  $N$  and bending moments  $M_y$  and  $M_z$  can then be computed based on the cross section area  $A$ , the Young's modulus of steel and the moments of inertia along axes  $y$  and  $z$ ,  $I_y$  and  $I_z$ :

$$N = E_{steel} A \varepsilon_G \quad (9)$$

$$M_y = E_{steel} I_y \chi_y \quad (10)$$

$$M_z = E_{steel} I_z \chi_z \quad (11)$$

Figure 16 illustrates the application of the above procedure to cross-section B (quarter span of the top horizontal element of the steel ring) to compute the axial force and bending moment along the weak axis at that cross section.

The development of the internal forces at cross-section B during the course of the test shows a consistent behavior, indicating that the steel profile is contributing to the lateral stiffness and strength of the reinforced masonry wall specimen. Combining the axial force and bending moments in that cross section, the maximum normal stress was 216 MPa, still clearly in the elastic range.

### Numerical analyses

Finite element models of the perforated walls were developed using the DIANA 9.2 software (De Witte and Kikstra 2007) to simulate the response of the tested masonry walls subjected to a combined state of constant vertical force and increasing in-plane imposed displacement. The main objective of these analyses was to calibrate the mechanical properties of the constituent materials as well as the boundary conditions between the steel ring and the surrounding masonry (in the case of the RMW specimen), taking as a reference the results of the experimental tests. The validation of the numerical models thus developed could ultimately serve as a way of extrapolating the conclusions of the experimental tests to other situations, e.g., different openings (location, size, etc.) or the absence of openings (solid wall, exemplified in 8.3).

## Numerical modeling of the unreinforced masonry wall (UMW)

### Numerical model

The rubble stone masonry material was described using a macro-modeling approach in which the masonry is treated as a composite, homogeneous, and isotropic material. This approach is more suitable for the study of old and irregular masonry walls with multiple leaves. Thus, the constitutive model adopted was the Total Strain Rotating Crack Model (RCM), which describes the tensile and compressive behavior of a material by means of a uniaxial stress-strain relationship and is suited to analyses predominantly governed by cracking or crushing of the material (De Witte and Kikstra 2007). The RCM allows a gradual correction of the initial crack direction as the crack plane can rotate during the analysis. Exponential and linear elastic stress-strain relations were used to describe the tensile and compressive behavior of the masonry, respectively, thereby disregarding the possibility of local crushing of the masonry, based on the observation that only shear and tensile phenomena were observed during the experimental tests.

The RC material was modeled as a linear isotropic elastic material since there was no evidence of non-linear behavior (cracking or crushing) of the stiff beam, the lintel and the footing. The mechanical properties were: Young's modulus of 30 GPa; Poisson ratio of 0.2; and specific weight of 25.0 kN/m<sup>3</sup>.

A regular mesh discretization was developed using eight-node quadrilateral isoparametric plane stress elements (50 x 75 mm) based on quadratic interpolation

and Gauss integration – CQ16M. The pre-compression level of 0.2 MPa was distributed through a set of nodes located at the top of the wall, in accordance with the experimental setup. The horizontal load was applied to the RC stiff beam nodes and the displacement was measured at the top of the same beam. In order to block the footing movements, all degrees of freedom of the nodes on the base were restrained: translation in x, translation in y and rotation in z. Concrete and masonry self-weights were also considered.

### Calibration and analysis

After the model definition was completed, a physical nonlinear monotonic analysis was performed to evaluate the in-plane behavior of the unreinforced masonry wall. The Quasi-Newton (Secant) BFGS iterative method was used with an internal energy convergence tolerance of 10<sup>-3</sup>. The experimental envelope as well as the obtained numerical curve after an iterative calibration process of some masonry properties can be seen in Figure 17. It is worth mentioning that the numerical model only provided the positive branch of the numerical curve, which was mirrored to the negative side to help in the calibration process.

Table 1 summarizes the calibrated masonry properties. Note that the Young's modulus obtained (800 MPa) is in accordance with the work carried out by Araújo (2014), in which a similar rubble stone masonry wall with hydraulic lime-based mortar was numerically cyclically tested to failure (with comparable pre-compression level). The tensile strength considered (0.02 MPa), however, is much higher than the average

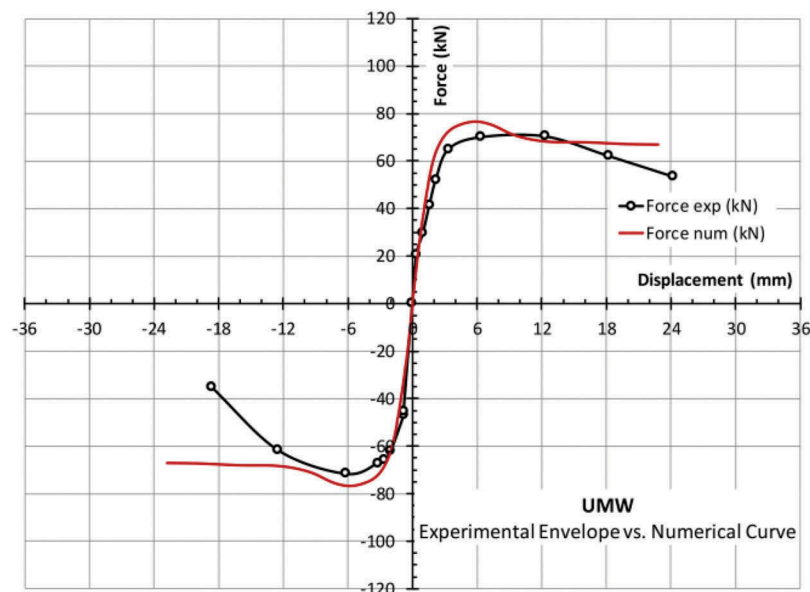


Figure 17. Experimental envelope and calibrated numerical curve (UMW).



**Table 1.** Calibrated masonry properties.

E (GPa)	Poisson Ratio	Density (kN/m <sup>3</sup> )	Tensile Strength (MPa)	Tensile Fracture Energy (Nmm/mm <sup>2</sup> )
0.80	0.20	18.35	0.02	0.02

resistance values determined for this type of masonry by other authors (Magenes et al. 2010; Milosevic et al. 2013). Actually, the tensile strength achieved matches the typical known values for masonry with aerial lime based mortars, e.g., 0.024 MPa obtained by Milosevic (Milosevic et al. 2013).

The analysis results of the UMW numerical model show that the in-plane behavior of this wall is in agreement with the experimental monotonic envelope, as the maximum capacity was correctly estimated (76.59 kN for a top lateral displacement of 5.67 mm) and the nonlinear force-displacement behavior conveniently fits the experimental curve.

The damage pattern was also evaluated for the UMW analysis by plotting the maximum principal strains distribution at failure (Figure 18, left). The UMW deformation state at collapse can be seen in Figure 18, right.

The crack pattern observed in the experimental test of this wall had diagonal cracking in both piers, consistent with the damage found in the numerical modeling results, which evidences shear failure by diagonal cracking.

#### **Numerical modeling of the reinforced masonry wall (RMW)**

The reinforced masonry wall model was based on that of the unreinforced masonry wall model, with the addition of the steel ring strengthening. The steel material of the ring profile was modeled as a linear isotropic elastic material with a Young's modulus of 210 GPa, and a Poisson ratio of 0.3. The UPN 160 steel profile was described by means of a two-node, two-dimensional beam element, L7BEN, and a predefined

U-shape was used (De Witte and Kikstra 2007). In addition, the mesh was refined in the vicinity of the opening so as to avoid excessive stress concentration near the window-frame-masonry wall connections and improve the convergence.

A physical nonlinear monotonic analysis was performed to evaluate the in-plane behavior of the reinforced model. The resulting numerical curve showed better approximation to the experimental hysteresis curve (Figure 19) when the steel frame was numerically tied to the surrounding masonry only at the compressed corners (neglecting the existence of connections at the other corners).

In spite of the numerical instabilities encountered, the model was able to capture the onset of the softening branch, permitting the identification of the value of the maximum horizontal force of 105.8 kN that occurred for a top horizontal displacement of 8.98 mm. The crack pattern exhibited by the numerical model is in reasonable agreement with that observed in the experimental tests, consisting of a diagonal cracking in both piers and influenced by the existence of the steel ring.

#### **Numerical modeling of a solid wall (SMW)**

As stated initially, the major assumption of the strengthening technique under study was that a strengthened wall with an opening should ultimately behave as if there were no opening. Considering that assumption a third numerical model, Solid Masonry Wall (SMW), was developed so as to confirm the effectiveness of the strengthened solution by extrapolation. The SMW model was based on the UMW model but without the opening and the concrete lintel. The damage pattern exhibited by the numerical model was that corresponding to diagonal shear, leading to a maximum applied horizontal load of 117.5 kN. This maximum load is possibly an overestimate of the strength of the solid wall since the masonry crushing phenomenon was not adequately addressed.

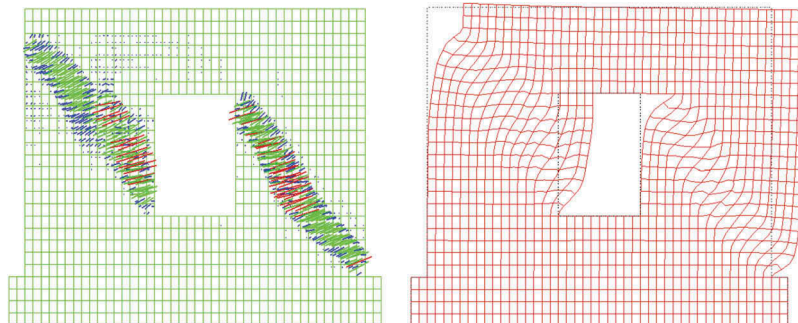


**Figure 18.** Damage pattern (left) and deformation state at failure (right) (UMW).

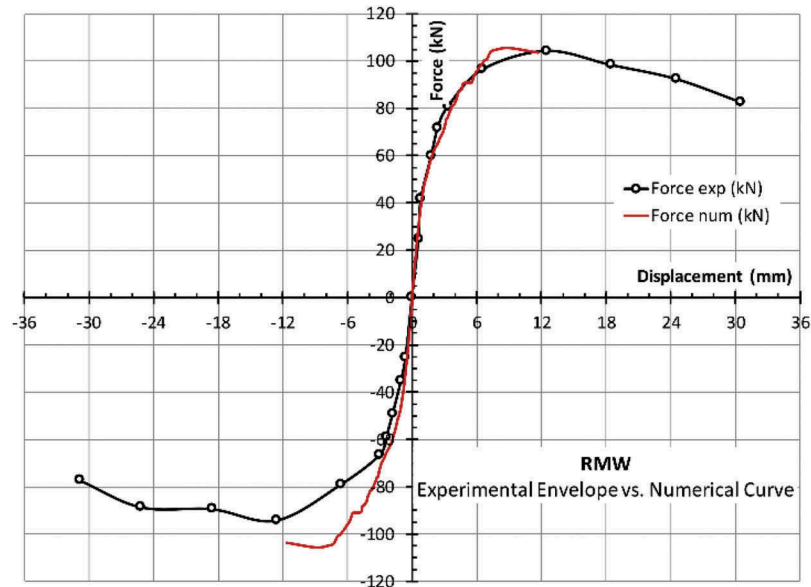


Figure 19. Experimental curve and calibrated numerical curve (RMW).

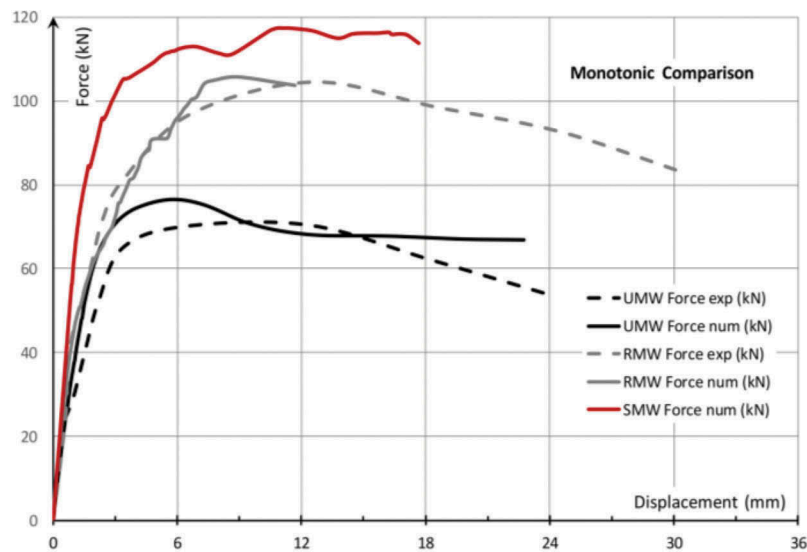


Figure 20. Force-displacement charts (all numerical and experimental models).

The comparison of all force-displacement charts, numerical and experimental, when available, is presented in Figure 20. The cyclic experimental charts were replaced by their positive monotonic envelopes.

The analysis of Figure 20 shows that notwithstanding the stiffness decrease exhibited by both the walls with openings, the peak strength exhibited by the RMW model is close to that of the solid wall model, albeit somewhat lower, thus showing that the major objective of the study was nearly reached.

## Conclusions

The present study was based on the assumption that placing a steel ring in the opening could stiffen and strengthen the masonry wall panel to a degree comparable to that of a wall without an opening, thereby delaying and modifying the well-known in-plane collapse mode for load bearing masonry walls involving damage to the piers.

To confirm the first assumption a series of experiments were performed in which two otherwise

equivalent masonry wall specimens, without (UMW) and with an internal steel ring (RMW), were cyclically tested to failure. The unreinforced masonry wall developed a typical shear mechanism with obvious diagonal cracking at the masonry piers on both sides of the opening, whereas the reinforced masonry wall developed a mixed shear-rocking mechanism with a more distributed crack pattern. The results of the experimental programme showed significant increases in the deformation capacity (25%) at failure and in the peak strength (+ 40%), and an even more significant increase of the cumulative dissipated energy (+ 147%) at failure. In spite of the limited number of tested wall specimens, the former results underline the worthiness of the underlying strengthening concept.

The experiments were preceded by the development of simplified analytical models and these have shown that the effectiveness of the strengthening solution greatly depends on the number, location, and types of constraints in the steel-ring-to-masonry-wall connection. Those simplified analytical models indicate that improving the former connection could reduce the flexural inertia of the steel ring profile enough to achieve the same stiffening effect.

The possibility of extrapolating the experimental results to other situations—different opening geometries and even the comparative analysis for a solid wall (i.e., without openings)—led to the development of numerical models with the DIANA 9.2 nonlinear finite element analysis program. These numerical models were initially developed for the tested masonry wall specimens, allowing the calibration of some parameters and of the type of constraints imposed at the steel-ring-to-masonry-wall connection. The comparison of the numerical vs. numerical results was satisfactory, particularly in terms of the peak strengths and corresponding displacements, stiffness, and damage patterns. A third numerical model, that of an equivalent solid masonry wall (without openings), was then developed to confirm the initial assumption in terms of the comparison between the behavior of a reinforced masonry wall and that of a solid masonry wall. This comparison showed encouraging results, indicating that the performance of the reinforced masonry wall comes close to that of the solid masonry wall, especially in terms of peak strength.

## Acknowledgments

The authors wish to thank CVF, Construtora de Vila Franca, Lda. for building the walls subjected to experimental tests and

HILTI Portugal - Produtos e Serviços, Lda. for supplying the threadbars and injectable adhesive anchors used in the steel-ring-to-masonry-wall connections.

## ORCID

Jorge Miguel Proença  <http://orcid.org/0000-0001-6308-7228>

António S. Gago  <http://orcid.org/0000-0002-2153-7953>

## References

- American Society for Testing and Materials (ASTM). 2002. *ASTM E2126-02a: Standard test methods for cyclic (reversed) load test for shear resistance of walls for buildings*. West Conshohocken, PA: ASTM.
- Araújo, A. 2014. Modelling of the Seismic Performance of Connections and Walls in Ancient Masonry Buildings. PhD Thesis, University of Minho, Portugal.
- Cakir, F., E. Uckan, J. Shen, B. S. Seker, and B. Akbas. 2015. Seismic damage evaluation of historical structures during Van earthquake, October 23, 2011. *Engineering Failure Analysis* 58 (1):249–66. doi:10.1016/j.engfailanal.2015.08.030.
- Comité Européen de Normalization (CEN). 2007. EN 1015-11:2007. *Methods of test for mortar for masonry – Part 11: Determination of flexural and compressive strength of hardened mortar*. Brussels: CEN.
- Cunha, D. 2013. Estudo de argamassas com base em cal hidráulica e suas aplicações. MSc Dissertation. Universidade de Aveiro. Portugal. (in Portuguese).
- De Witte, F. C., and W. P. Kikstra. 2007. *Diana finite element analysis user's manual. Release 9.2. material library*. Delft: TNO DIANA.
- Fardis, M. N., Carvalho, E., Elnashai, A., Faccioli, E., Pinto, P., and Plumier, A. 2005. Designers' Guide to EN 1998-1 and 1998-5. Eurocode 8: Design Provisions for Earthquake Resistant Structures. In H. Gulvanessian, Ed. UK: Thomas Telford.
- Kalali, A., and M. Kabir. 2012. Cyclic behavior of perforated masonry walls strengthened with glass fiber reinforced polymers. *Scientia Iranica* 19(2):151–65. doi:10.1016/j.scient.2012.02.011.
- Magenes, G., A. Penna, A. Galasco, and M. Rota. 2010. Experimental characterisation of stone masonry mechanical properties. In Proceedings of the 8th International Masonry Conference, Dresden, Germany.
- Marques, R., P. Lamego, P. B. Loureço, and M. L. Sousa. 2017. Efficiency and cost-benefit analysis of seismic strengthening techniques for old residential buildings in Lisbon. *Journal of Earthquake Engineering* 1–36. doi:10.1080/13632469.2017.1286616.
- Mendes, N., and P. B. Lourenço. 2015. Seismic vulnerability of existing masonry buildings: Nonlinear parametric analysis. In *Seismic assessment, behavior and retrofit of heritage buildings and monuments. Computational methods in applied sciences*, I. N. Psycharis, S. J. Pantazopoulou, and M. Papadrakakis, edited by, 37. Switzerland: Springer.
- Milosevic, J., A. Gago, M. Lopes, and R. Bento. 2013. Experimental assessment of shear strength parameters on

- rubble stone masonry specimens. *Construction and Building Materials* 47:1372–80. doi:10.1016/j.conbuildmat.2013.06.036.
- Milosevic, J., A. Gago, M. Lopes, and R. Bento. 2015. In-plane seismic response of rubble stone masonry specimens by means of static cyclic tests. *Construction and Building Materials* 82:9–19. doi:10.1016/j.conbuildmat.2015.02.018.
- Mortar Industry Association (MIA). 2015. *Data sheet 19 - A guide to BS EN 998-1 and BS EN 998-2. Issue 3*. MPA (Mineral Products Association): London, UK.
- Pelà, L., P. Roca, and A. Aprile. 2017. Combined in-situ and laboratory minor destructive testing of historical mortars. *International Journal of Architectural Heritage*. doi:10.1080/15583058.2017.1323247.
- Politecnico di Milano (POLIMI). 2010. Inventory of earthquake-induced failure mechanisms related to construction types, structural elements, and materials. Deliverable 3.1. In *New integrated knowledge based approaches to the protection of cultural heritage from Earthquake-induced Risk (NIKER)*. Milan, Italy: POLIMI.
- Portuguese Institute for Quality (IPQ). 2010. *NP EN 998-1:2010 Specification for masonry mortars -Part 1: Plastering mortars for interior and exterior*. in Caparica, Portuguese: IPQ.
- Simões, A. G., J. G. Appleton, R. Bento, J. V. Caldas, P. B. Lourenço, and S. Lagomarsino. 2017. Architectural and structural characteristics of masonry buildings between the 19th and 20th Centuries in Lisbon, Portugal. *International Journal of Architectural Heritage* 11 (4):457–74. doi:10.1080/15583058.2016.1246624.
- Vanin, A., and P. Foraboschi. 2012. In-plane behavior of perforated brick masonry walls. *Materials and Structures* 45:1019–34. doi:10.1617/s11527-011-9814-x.
- Vilas Boas, A. 2017. Reforço sísmico de edifícios de alvenaria mediante a introdução de caixilhos metálicos nos vãos. MSc Dissertation. Instituto Superior Técnico, Universidade de Lisboa. Portugal. (in Portuguese).